

High Areal Capacity Anode Enabled by Enhanced Charge Transport on Self-Supported Spindle-Like Carbon Nanofiber Architecture of CTAB-Treated Geothermal Silica Waste

Faiq Haidar Hamid,^[a] Yuyun Irmawati,^[b, c] Aisyah Nur Estri,^[a] Aldan Hadziq Haidar,^[a] and Afriyanti Sumboja^{*[a]}

High areal-capacity anodes are crucial for compact and energy-dense lithium-ion batteries. Nevertheless, thick slurry cast on current collectors often leads to sluggish charge transport and poor cycle stability. This study addresses these issues by developing self-supported spindle-like silica-carbon nanofiber architectures via electrospinning. Cetyltrimethylammonium bromide (CTAB) surfactant is employed to modify the surface potential of geothermal silica waste nanoparticles, enhancing their dispersibility in electrospinning solution and producing fully encapsulated silica nanoparticles within spindle-like carbon nanofibers ($\text{SiO}_2\text{-CTAB@CNF}$). Unlike thick slurry-based designs, spindle-like structures can serve as spacers, creating efficient pathways for electrolyte infiltration across the anode thickness.

Consequently, $\text{SiO}_2\text{-CTAB@CNF}$ balances optimal porosity (34%) toward high active material loading (9.5 mg cm^{-2}), establishing low tortuosity (τ : 2) and high coefficient of diffusivity. The half-cell $\text{SiO}_2\text{-CTAB@CNF}$ battery delivers a notable areal discharge capacity of 4 mAh cm^{-2} , meeting commercial high-areal capacity targets. The full-cell $\text{SiO}_2\text{-CTAB@CNF} \parallel \text{LFP}$ achieves high discharge capacity of 3.6 mAh cm^{-2} at 0.1 mA cm^{-2} . Even under higher areal current value (0.3 mA cm^{-2}), the full-cell battery can deliver capacity of 2.58 mAh cm^{-2} and remain stable after 100 cycles. This work highlights the use of advanced nanostructures and geothermal silica waste to produce sustainable and high-areal capacity lithium-ion batteries.

Introduction

The growing global demand for electricity drives the need to advance lithium-ion batteries with enhanced storage capabilities. High-areal capacity anodes offer several benefits to support this purpose, including high energy density and potentially simpler cell designs due to their compactness.^[1] Commercially targeted high-areal capacity anodes require substantial value of active material loadings and thick-layered electrodes (i.e., $2\text{--}4 \text{ mAh cm}^{-2}$ and $>100 \mu\text{m}$), thereby increasing the proportion of electrochemically active over inactive components in the electrode.^[2] For slurry-based electrodes, in particular, this condition may cause several issues, such as electrode cracking,^[3] delamination of active materials from current collector,^[4] and sluggish ion transport as well as slow electron conduction resulting from the high tortuosity, long

diffusion distances, and high resistances.^[5] These conditions reduce the effective use of active materials, resulting in low areal capacity and unstable performance over cycles. Hence, designing anodes with high-areal capacity and stable cycle performance is essential.

Silicon and silica (SiO_2) offer substantial theoretical capacities of 3578 and 1965 mAh g^{-1} , respectively. These materials have emerged as promising alternatives to conventional graphite-based anodes, which deliver a low capacity of 372 mAh g^{-1} for high-performance applications.^[6] Nevertheless, their poor electrical conduction properties and high-volumetric changes still hinder their practical applications in lithium-ion batteries.^[7] Nanostructuring^[8] and carbon-coating^[9,10] have been demonstrated as promising approaches to address those issues. However, most reported studies have only shown thin Si and SiO_2 -based electrodes with low active material loadings ($1\text{--}2 \text{ mg cm}^{-2}$), providing a limited areal capacities ($<1.5 \text{ mAh cm}^{-2}$), which could lead to different performance outcomes when scaled up to higher loading anodes.^[11\text{--}14]

Some works have been explored to develop Si or SiO_2 -based anodes with high areal capacity. For example, a slurry-based Si/ SiO_2 /graphite electrode on Cu foil was reported to deliver approximately 2 mAh cm^{-2} of areal capacity with active material loading of 4 mg cm^{-2} .^[15] To overcome the prolonged electron transfer from active material to current collector in conventional planar thick electrodes, 3D porous nickel foam was utilized as current collector, yielding a Si-based anode with 7.7 mAh cm^{-2} of areal capacity.^[16] Furthermore, incorporating SiO_2 nanoparticles into MXene layers mitigated the volumetric expansion

[a] F. Haidar Hamid, A. Nur Estri, A. Hadziq Haidar, A. Sumboja
Materials Science and Engineering Research Group, Faculty of Mechanical and Aerospace Engineering, Institut Teknologi Bandung, Jl. Ganesa 10 Bandung 40132, Indonesia
E-mail: sumboja@itb.ac.id

[b] Y. Irmawati
Doctoral Program of Nanosciences and Nanotechnology, Graduate School, Institut Teknologi Bandung, Jl. Ganesa 10, Bandung 40132, Indonesia

[c] Y. Irmawati
Research Center for Nanotechnology Systems, National Research and Innovation Agency (BRIN), Tangerang Selatan 15314, Indonesia

 Supporting information for this article is available on the WWW under <https://doi.org/10.1002/batt.202500021>

of SiO_2 and improved electron transfer, producing an anode with 2.16 mAh cm^{-2} of areal capacity at 2.58 mg cm^{-2} of active material loading.^[17] Despite that, these referenced studies still employ slurry-based technology and use heavy current collectors (e.g., ~ 9 and $\sim 35 \text{ mg cm}^{-2}$ for Cu-foil and nickel foam), increasing batteries' weight and limit their total energy density.^[18]

Self-supporting electrodes have been increasingly favored to eliminate the need for inactive binders and heavy current collectors.^[19] Electrospinning has been recognized as an effective synthesis method for producing self-supporting electrodes.^[20] This method can also create pore structures from the gaps between the entangled nanofibers. The pore serves as electrolyte infiltration pathways, producing highly accessible storage sites and shortening ion-diffusion distances.^[21] Interconnected 1D structures can also serve as conductive networks, enabling faster electron conduction and improving ion transport throughout the electrode thickness.^[22] Most reported polyacrylonitrile (PAN)-based electrospinning solutions can also produce nitrogen-doped carbon nanofibers.^[21,22] Nitrogen doping enhances the conductivity of the carbon matrix, creates localized negative charges that facilitate Li-ion transfer, and introduces defects that increase active Li^+ storage sites, ultimately improving Li storage performance.^[9,23] All these benefits make electrospinning a potential technique to generate high areal capacity anodes.^[19] However, in contrast to research on low mass-loading electrospun Si/SiO_2 -based anodes,^[18,24–28] comprehensive analysis of employing electrospinning to produce high active material loading with high areal capacity of Si/SiO_2 -based anodes is still limited.

Furthermore, utilizing waste-derived SiO_2 precursors is an attractive option in terms of cost and environmental sustainability.^[29] Geothermal silica waste, which is abundantly produced in geothermal power plants, is a valuable resource due to its high SiO_2 content ($\sim 97\%$).^[30] Nevertheless, unlike TEOS precursor,^[31] integrating SiO_2 powder into nanofiber via electrospinning is challenging due to the tendency of SiO_2 particles to form unencapsulated SiO_2 particles on the nanofiber matrix.^[24] The unencapsulated SiO_2 particles would diminish contact between conductive carbon nanofibers and non-conductive SiO_2 , obstructing effective electron transfer.^[2,32] Furthermore, unencapsulated SiO_2 is prone to uncontrolled volume expansion, leading to unstable SEI formation and compromising long-term capacity retention due to continuous capacity loss.^[33]

Herein, we develop high areal-capacity anodes by fabricating self-supported spindle-like silica-carbon nanofiber architecture via electrospinning. Building on surface modification strategies known to enhance material processability,^[34–36] geothermal silica waste was treated with cetyltrimethylammonium bromide (CTAB) to address the issue of unencapsulated silica nanoparticles. This process allowed us to modify the surface potential of silica nanoparticles, enabling them to disperse well in electrospinning solution, resulting in fully encapsulated SiO_2 nanoparticles within nanofibers with uniform spindle-like structures (SiO_2 -CTAB@CNF). This spindle-like structure functions as a spacer, leading to higher porosity and lower

tortuosity, which is beneficial in producing highly accessible storage sites and efficient Li-ion diffusion throughout the anode thickness. Fully encapsulated SiO_2 within spindle-like structures also provide better conductive networks, improving electron transfer. Consequently, SiO_2 -CTAB@CNF anode can deliver a high areal capacity of 4 mAh cm^{-2} under high material loading (9.5 mg cm^{-2}). From post-mortem examination, spindle-like structure also undergoes minimal morphological changes, mitigating the volume expansion of SiO_2 nanoparticles. Furthermore, pairing SiO_2 -CTAB@CNF anode with commercial LFP cathode results in a high discharge capacity of 3.6 mAh cm^{-2} (0.1 mA cm^{-2}) and good stability at a higher areal current value of 0.3 mA cm^{-2} for up to 100 cycles, confirming its potential application.

Experimental

Fabrication of Purified SiO_2

Geothermal silica waste was obtained from Geodipa Power Plant (Wonosobo, Indonesia). The silica waste was first leached using 25% H_2SO_4 (Honeywell Fluka) at 80°C for 3 h to dissolve contaminants. The leached silica was then subjected to multiple rinses with DI water before drying in an oven. Purification process was continued by dissolving the leached silica in 3 M NaOH (Emsure) at 70°C (3 h). Subsequently, 1 M HCl (Honeywell Fluka) was added gradually until the pH was neutral, followed by an 18-h period of precipitation resting. After that, the obtained white precipitate was washed three times using boiling DI water and dried at 100°C to form SiO_2 chunks. The chunks were then ball-milled, resulting in purified fine silica powder.

Fabrication of SiO_2 -CTAB@CNF

1 g of purified fine silica powder was dispersed into 500 mL of aqueous CTAB mixture (CTAB: 3 g, Sigma Aldrich). The mixture was vigorously stirred for 3 h before being filtered to obtain SiO_2 -CTAB powder. Polyacrylonitrile (PAN, Sigma Aldrich) was dissolved to obtain 8 wt% PAN solution in N, N-dimethylformamide (DMF, Sigma Aldrich). SiO_2 -CTAB powder was then dispersed in PAN solution (1:10 of w/w ratio), resulting in SiO_2 -CTAB@PAN electrospinning solution. Electrospinning process was performed at relative humidity (RH) of 60%, with an infusion rate of $0.030 \text{ mL min}^{-1}$ under 12 kV applied voltage. The resulting SiO_2 -CTAB@PAN nanofiber mat was transferred into an ambient air furnace (280°C , 2 h) for thermal stabilization, followed by a 700°C carbonization process (2 h, N_2). This process yielded a self-supported SiO_2 -CTAB@CNF anode. For comparison, a sample without CTAB treatment was also prepared using a similar procedure and indexed as SiO_2 @CNF.

Material Characterization

Fourier transform infrared (FTIR) spectra were collected using Bruker Alpha II. Zeta potential analysis was conducted using Nano Particle Analyzer Horiba SZ-100. X-ray diffraction (XRD) patterns were recorded on Bruker D8 Advanced. X-ray photoelectron spectroscopy (XPS) data were gathered using a Kratos Axis Supra⁺. Hitachi SU3500 was used to obtain scanning electron microscopy (SEM) images and the elemental mapping of energy-dispersive spectroscopy (EDS). Tecnai G2 20S-Twin was utilized to obtain the

transmission electron microscopy (TEM) images. Themys One was utilized to obtain thermogravimetric (TG) data. Porosity of nano-fiber mats was determined using weighing method adopting the previous study.^[20] Fiber mats with 10 mm width and 20 mm gauge length were prepared for tensile testing using the Instron 5985 machine at a grip separation rate of 0.2 mm min⁻¹.

Results and Discussion

Figure 1a illustrates the fabrication of self-supported SiO₂-CTAB@CNF anode derived from geothermal silica waste. Silica waste was first purified using H₂SO₄ and NaOH treatment,^[30] before being ball-milled into fine silica powder. Subsequently, the fine silica powder was treated using CTAB. The existence of CTAB on the treated sample was confirmed by FTIR peaks at 2845 and 2917 cm⁻¹, corresponding to –CH₂ vibrations of CTAB (Figure S2, Supporting Information).^[37] Zeta potential analysis reveals that the surface potential of CTAB-treated SiO₂ shifts to a more positive value compared to pristine SiO₂ (Figure S3,

Supporting Information), which is related to the electrostatic stabilization of SiO₂-CTAB within PAN electrospinning solution (Figure 1b).^[36] This results in better dispersibility of SiO₂ in PAN solution. After electrospinning, the obtained SiO₂-CTAB@PAN nanofiber mat was subjected to stabilization and carbonization steps, producing self-supported SiO₂-CTAB@CNF anode. A similar sample without CTAB treatment was also prepared and indexed as SiO₂@CNF.

Morphological features of the carbonized electrospun mats were analyzed using SEM images. SiO₂@CNF and SiO₂-CTAB@CNF feature randomly oriented stacked nanofibers that generate pores from the gaps and spaces between fibers (Figure 1c,d). SiO₂@CNF shows uneven surfaces of nanofibers with SiO₂ clusters not encapsulated inside nanofibers (inset Figure 1c). The formation of unencapsulated SiO₂ nanoparticles on SiO₂@CNF can be related to fast separation between SiO₂ and PAN solution prior to jet solidification that may be caused by the poor dispersibility of untreated SiO₂ within the electrospinning solution.^[38] Differently, SiO₂-CTAB@CNF shows smooth fiber surfaces with spindle-like structures, wherein SiO₂ nano-

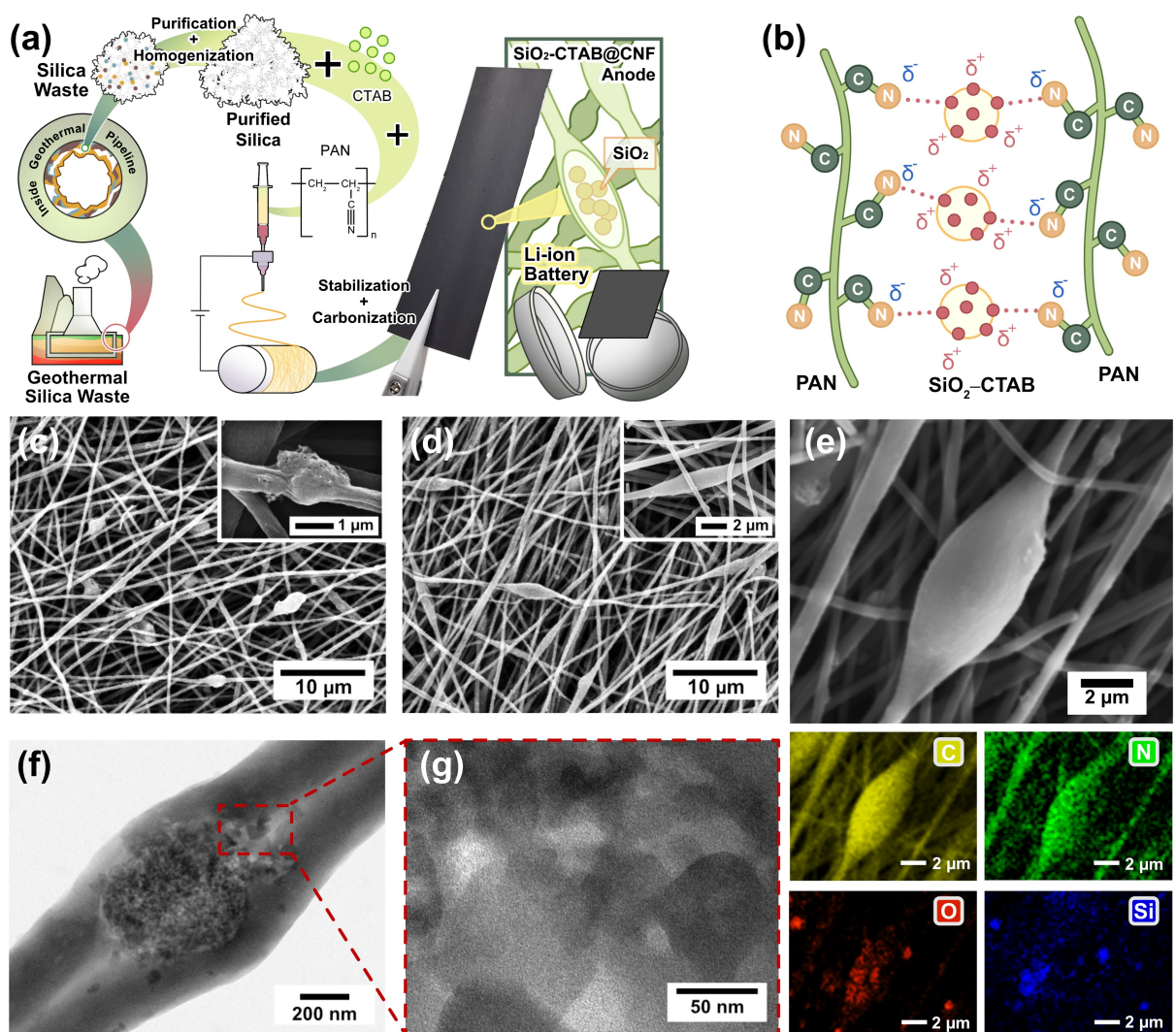


Figure 1. (a) Illustration production of binder-free self-supporting SiO₂-CTAB@CNF anode. (b) Schematic interaction between CTAB-treated SiO₂ and PAN in the electrospinning solution. SEM images of (c) SiO₂@CNF and (d) SiO₂-CTAB@CNF. (e) EDS mapping of SiO₂-CTAB@CNF. (f, g) TEM images of SiO₂-CTAB@CNF.

particles remain enclosed within nanofibers (inset Figure 1d). Introducing CTAB to PAN electrospinning solution increased its conductivity while decreasing the viscosity.^[39] This condition affects the stability of the spinning jet, which may result in the formation of spindle-like structures.^[40,41] Furthermore, the better dispersibility of CTAB-treated SiO_2 in the electrospinning solution also allows SiO_2 nanoparticles to remain enclosed within spindle-like nanofibers.

EDS mapping verified the presence of C, O, N, and Si on both anodes. $\text{SiO}_2@\text{CNF}$ anode displayed Si and O signals of various sizes, suggesting that SiO_2 nanoparticles form clusters of different sizes on the carbon nanofiber surface (Figure S6, Supporting Information). The bright spot color suggests that CNF does not encapsulate the clusters. In contrast, the $\text{SiO}_2-\text{CTAB}@\text{CNF}$ displayed a consistent spindle-like structure where SiO_2 nanoparticles were evenly encapsulated. The vivid Si and O signals suggest that SiO_2 nanoparticles are enclosed within the spindle-like carbon nanofibers (Figure 1e). Notably, this spindle-like structure with SiO_2 nanoparticles inside also serves as a spacer that widens the slits and gaps between nanofibers.^[42] This creates a higher porosity of $\text{SiO}_2-\text{CTAB}@\text{CNF}$ (34%) compared to $\text{SiO}_2@\text{CNF}$ (28%). Increased pore architecture within the anode can enhance the accessible storage sites and facilitate better electrolyte infiltration as well as Li-ion transport.^[19,21]

TEM analysis was then used to analyze the internal features of spindle-like structures. As expected, the spindle structure comprises SiO_2 nanoparticles with a size of 100–150 nm (Figure 1f,g). The SiO_2 nanoparticles enclosed within spindle-like structure would benefit from reducing the exposed surface of SiO_2 nanoparticles from electrolytes, which could stabilize SEI formation and thus improve battery cycle performance.^[36] The fully encapsulated SiO_2 within nanofibers can also mitigate volumetric expansion of SiO_2 nanoparticles over repeated charging and discharging, enabling long-cycle stability.^[43] Moreover, interconnected carbon nanofibers with fully encapsulated SiO_2 structures facilitate conductive networks that could boost the electrochemical performance by providing continuous electron transfer to the non-conductive SiO_2 .^[44]

The anodes' phase structures were then analyzed using XRD. Both $\text{SiO}_2@\text{CNF}$ and $\text{SiO}_2-\text{CTAB}@\text{CNF}$ showed similar diffraction patterns, in which two broad peaks around 26° and 44° matched with carbon peaks (Figure 2a), indicating successful carbonization of PAN precursors.^[45] The overlapping peak of SiO_2 and carbon at about 26° complicates the identification of SiO_2 .^[46] The existence of SiO_2 has been confirmed via EDS mapping and the following XPS analysis. Surface chemical properties of $\text{SiO}_2-\text{CTAB}@\text{CNF}$ were examined using XPS. C 1s spectra of $\text{SiO}_2-\text{CTAB}@\text{CNF}$ (Figure 2b) were deconvoluted into C=O, C–O, C–N, and C–C at about 288.0, 286.3, 285.4, and 284.4 eV.^[47,48] The C–N peak indicates the existence of nitrogen-doped carbon from the decomposition of PAN during the carbonization process.^[49]

Nitrogen doping is further confirmed by N 1s spectra (Figure 2c), which reveals the presence of nitrogen-containing carbon structures, including pyridinic-N (397.8 eV), graphitic-N (400.3 eV), and pyrrolic-N (399.0 eV).^[50] Oxidized-N peak is also

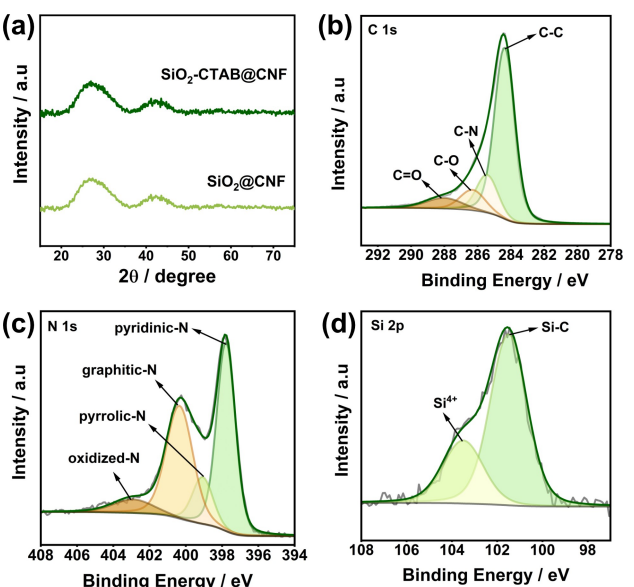


Figure 2. (a) X-ray diffractogram of $\text{SiO}_2@\text{CNF}$ and $\text{SiO}_2-\text{CTAB}@\text{CNF}$. (b–d) High-resolution XPS spectra of $\text{SiO}_2-\text{CTAB}@\text{CNF}$, including C 1s, N 1s, and Si 2p.

observed at 402.9 eV. Incorporating nitrogen doping into carbon matrix can generate defects, provide storage sites, and improve conductivity, thereby enhancing the anode performance.^[24] Si 2p spectra of $\text{SiO}_2-\text{CTAB}@\text{CNF}$ (Figure 2d) show Si^{4+} peak (103.5 eV) that confirms the SiO_2 phase.^[51,52] Another peak at 101.5 eV, indexed as Si–C, indicates a strong interaction between SiO_2 and carbon nanofibers.^[53,54] Combined with the embedded SiO_2 nanoparticles inside the fibers, this structure can enhance charge transfer and preserve structural integrity by avoiding excessive volume expansion of SiO_2 nanoparticles. TG analysis further revealed that $\text{SiO}_2@\text{CNF}$ and $\text{SiO}_2-\text{CTAB}@\text{CNF}$ anodes have the same SiO_2 content of about 20 wt% (Figure S7, Supporting Information). Additionally, the tensile properties of both anodes align with those previously reported $\text{Si}/\text{SiO}_2@\text{CNF}$ anodes, indicating their suitability for self-supporting anode applications (Figure S8, Supporting Information).^[55,56]

Electrochemical performances of self-supported anodes then assessed by directly employing $\text{SiO}_2@\text{CNF}$ and $\text{SiO}_2-\text{CTAB}@\text{CNF}$ in a half-cell configuration without additional conditioning or a current collector. CV measurements were first used to study the redox reactions in the anodes. During the first CV scan at a low scan rate (0.1 mVs⁻¹, inset Figure 3a,b), cathodic peaks corresponding to SEI formation were observed at 1.2 V for $\text{SiO}_2@\text{CNF}$ and 0.57 V for $\text{SiO}_2-\text{CTAB}@\text{CNF}$ anode.^[57,58] The low potential value for SEI formation promotes a more controlled SEI growth, resulting in a dense, less thick, and more robust SEI layer.^[57] This may contribute to higher coulombic efficiency and improved capacity retention on $\text{SiO}_2-\text{CTAB}@\text{CNF}$ anode.^[10,57] Cathodic peak at 0.01 V observed in both samples is related to the alloying process involving Li^+ and Si/SiO_2 .^[57,59] This peak matches the broad anodic peak observed at 0.3 and

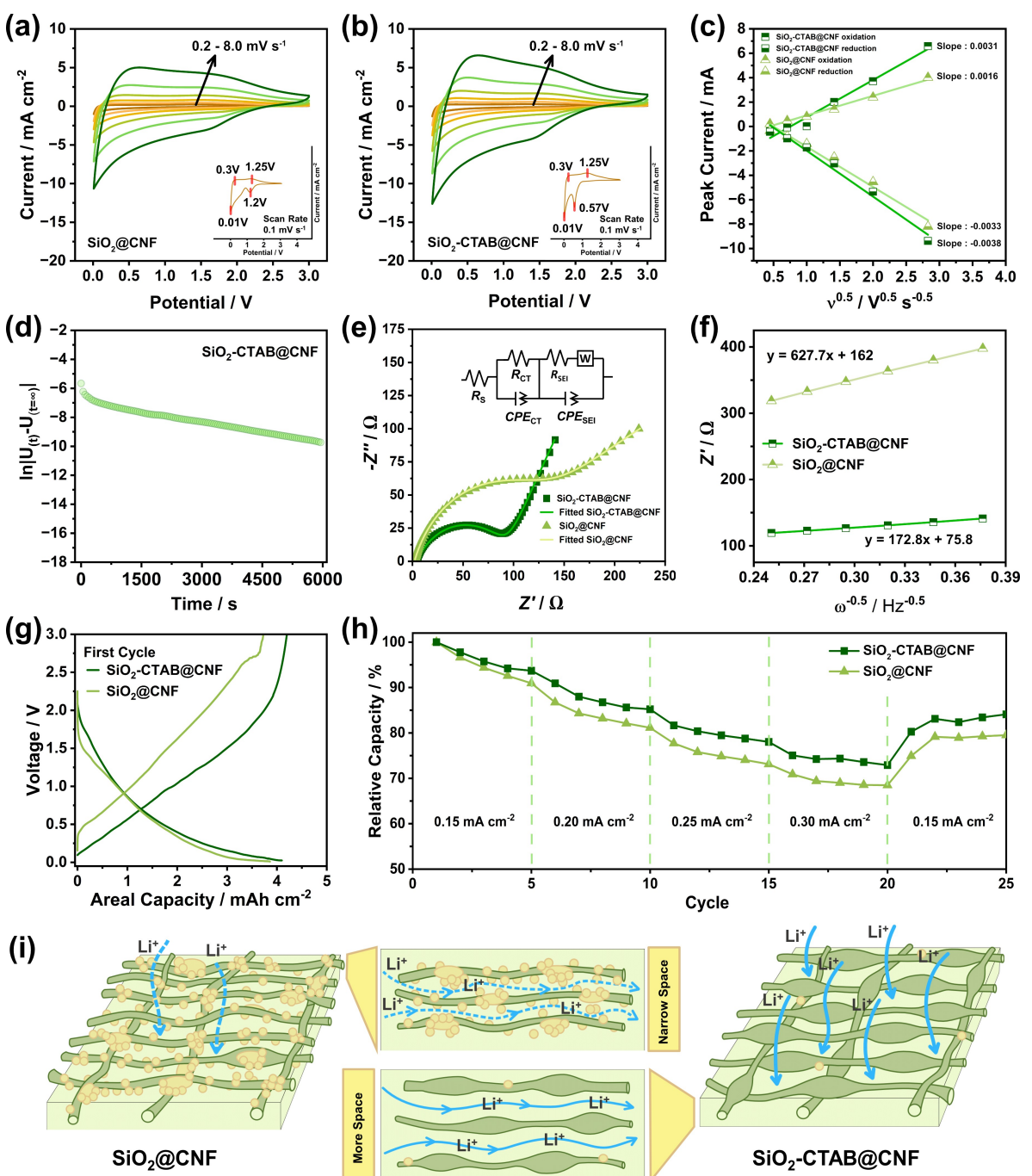


Figure 3. Performance evaluation of $\text{SiO}_2\text{-CNF}$ and $\text{SiO}_2\text{-CTAB@CNF}$: (a,b) cyclic voltammetry curve at various scan rates, (c) linear fitting of cathodic/anodic peak currents against the square root of scan rates. (d) DC-depolarization curve of $\text{SiO}_2\text{-CTAB@CNF}$, (e) EIS curve, and (f) its linearly fitted of its Z' against $\omega^{-0.5}$. (g) Voltage profile from the first cycle at 0.2 mA cm^{-2} and (h) cycling capability of $\text{SiO}_2\text{-CNF}$ and $\text{SiO}_2\text{-CTAB@CNF}$ at different areal current values. (i) Illustration of the spindle-like structure serving as spacers in improving Li-ion diffusion.

1.25 V, related to the dealloying process of Li^+ from amorphous Si/SiO_2 .^[59,60]

CV curves were later captured from different scanning rates to investigate the electrode's kinetics further (Figure 3a,b). $\text{SiO}_2\text{-CTAB@CNF}$ shows a higher current response than $\text{SiO}_2\text{-CNF}$ at 0.2–8.0 mV s⁻¹, which corresponds to higher accessible storage sites, faster Li-ion diffusion, and electron transfer of $\text{SiO}_2\text{-CTAB@CNF}$.^[61] The highly accessible storage site of $\text{SiO}_2\text{-$

CTAB@CNF aligns with its higher porosity, as also proven by its higher double-layer capacitance than $\text{SiO}_2\text{-CNF}$ (Figure S10, Supporting Information). The straight-line gradient obtained from plotting CV peak current against the square root of scan rate ($v^{1/2}$) is then used to perceive the diffusion kinetics of Li-ions.^[62] Figure 3c shows that $\text{SiO}_2\text{-CTAB@CNF}$ has a larger slope value compared to $\text{SiO}_2\text{-CNF}$, indicating its greater Li-ion diffusion capability. Employing the DC-depolarization method

(Figure 3d),^[2] the high Li-ion diffusion of $\text{SiO}_2\text{-CTAB@CNF}$ can be attributed to its lower tortuosity value (τ : 2) than $\text{SiO}_2\text{@CNF}$ (τ : 4, Figure S11, Supporting Information), enabling faster Li-ion transport across the anode thickness. The tortuosity value of $\text{SiO}_2\text{-CTAB@CNF}$ is also comparable to that of lithium battery electrodes featuring aligned pore topologies (τ : 1.5–1.9),^[63–65] highlighting the benefits of spindle-like structure in producing low-tortuosity anode. The low tortuosity of $\text{SiO}_2\text{-CTAB@CNF}$ reconfirms the advantages of spindle-like structures in increasing the spaces between nanofibers, enhancing Li-ion transport (Figure 3i). EIS curves were then tested within the 100 kHz to 10 mHz frequency range to examine the electrochemical impedance characteristics of the assembled self-supported anode batteries. Figure 3e shows a higher charge transfer capability of $\text{SiO}_2\text{-CTAB@CNF}$, as proven by its lower charge transfer resistance (R_{CT} : 91.26 Ω) than $\text{SiO}_2\text{@CNF}$ (119.76 Ω). This trend highlights the benefit of fully enclosed spindle-like structures that facilitate continuous electron transfer and Li-ions transport to the non-conductive SiO_2 .^[44,66] Additionally, $\text{SiO}_2\text{-CTAB@CNF}$ exhibits a much lower SEI resistance value (R_{SEI} : 37.21 Ω) compared to $\text{SiO}_2\text{@CNF}$ (353.19 Ω), detailed in Table S1, Supporting Information. Lower R_{SEI} of $\text{SiO}_2\text{-CTAB@CNF}$ may result from its spindle-like structure, which prevents direct interaction between silica and electrolyte,^[67,68] minimizing excessive SEI formation.

Li-ion diffusion coefficients ($D_{\text{Li}^+}\text{[EIS]}$) were also analyzed by evaluating EIS curves at low-frequency Warburg impedance region.^[27] The real impedance (Z') was plotted against the inversed square root of angular frequencies ($\omega^{-0.5}$) to obtain the linear slope values, referred to as Warburg coefficient (σ). From Figure 3f, $\text{SiO}_2\text{-CTAB@CNF}$ shows σ values of 172.8 $\Omega \text{ Hz}^{-0.5}$, much lower than that for $\text{SiO}_2\text{@CNF}$ (627.7 $\Omega \text{ Hz}^{-0.5}$). Since σ value is inversely proportional to $D_{\text{Li}^+}\text{[EIS]}$,^[9] the lower σ of $\text{SiO}_2\text{-CTAB@CNF}$ indicates its higher D_{Li^+} than $\text{SiO}_2\text{@CNF}$. Using similar calculation parameters from the previously reported Si/SiO_x@CNF anode,^[60] the calculated $D_{\text{Li}^+}\text{[EIS]}$ for $\text{SiO}_2\text{-CTAB@CNF}$ is $4.99 \times 10^{-13} \text{ cm}^2 \text{ s}^{-1}$. Despite having a high active material loading, the $D_{\text{Li}^+}\text{[EIS]}$ of $\text{SiO}_2\text{-CTAB@CNF}$ remains equivalent to or even exceeds that of reported anodes with lower active material loading, such as PVP-g-SiO₂@CNF ($4.72 \times 10^{-14} \text{ cm}^2 \text{ s}^{-1}$)^[60] and SiO₂@CS/SiO₂-CNF (2.51×10^{-14}).^[56] This confirms the advantages of spindle-like structures in enhancing Li-ion transport.

Combining the advantages of large accessible storage sites, improved Li^+ diffusion, and fast electron conduction, $\text{SiO}_2\text{-CTAB@CNF}$ anode shows voltage profile with a higher discharge platform (Figure 3g) and results in areal capacity of 4 mAh cm^{-2} at 0.2 mA cm^{-2} ($\sim 435 \text{ mAh g}^{-1}$). This value is higher than that for $\text{SiO}_2\text{@CNF}$ (3.8 mAh cm^{-2}), which also stands out among other research on low active material loading electrospun Si/SiO_x-based anodes (Table S2, Supporting Information). Additionally, the areal capacity of $\text{SiO}_2\text{-CTAB@CNF}$ is comparable to some reported high-areal capacity of Si/SiO_x-based anodes that mainly use slurry-based technology with heavy current collectors (Table S3, Supporting Information). Cycling capability of $\text{SiO}_2\text{@CNF}$ and $\text{SiO}_2\text{-CTAB@CNF}$ anode under various areal current values was then examined using a rate capability test. Compared to capacity at 0.15 mA cm^{-2} , $\text{SiO}_2\text{-CTAB@CNF}$ can

maintain 75% of its capacity at 0.30 mA cm^{-2} (Figure 3h), higher than $\text{SiO}_2\text{@CNF}$ (70%). This highlights the ability of spindle-like structures with fully enclosed SiO_2 nanoparticles to facilitate better electron conduction frameworks, as also in accordance with the EIS results.

The galvanostatic charge-discharge performance of the self-supported anodes was carried out under 0.2 mA cm^{-2} to assess their cycling stability. During the first 15 cycles (Figure 4a), $\text{SiO}_2\text{@CNF}$ experienced a significant capacity depletion from 3.8 to 1.9 mAh cm^{-2} , more pronounced than $\text{SiO}_2\text{-CTAB@CNF}$ (from 4 to 3.5 mAh cm^{-2}). The capacity depletion of $\text{SiO}_2\text{@CNF}$ continues to occur, resulting in capacity retention of about 30% only by the 30th cycle. Conversely, $\text{SiO}_2\text{-CTAB@CNF}$ anode maintained a remarkable 80% of its first-cycle areal capacity (3.2 mAh cm^{-2}) throughout 125 cycles of stability test. This enhanced stability of $\text{SiO}_2\text{-CTAB@CNF}$ can be ascribed to the spindle-like architecture, which effectively maintains the volume expansion of SiO_2 nanoparticles, preventing structural collapse during repeated volume expansion and contraction throughout the cycling test.^[31,56]

To grasp the visual detail of the anode's deterioration after the stability test, the cells were dismantled and washed using dimethyl carbonate to allow the post-mortem SEM examination. After the stability test, $\text{SiO}_2\text{@CNF}$ anode (Figure 4b) depicts blister-like structures along the nanofiber. This structure may result from the uncontrolled volume expansion of unencapsulated silica nanoparticles, resulting in the nanoparticle pullout.^[69,70] In contrast, post-mortem SEM images of $\text{SiO}_2\text{-CTAB@CNF}$ (Figure 4c) show a well-maintained spindle-like and nanofiber morphology, demonstrating its high structural stability. Furthermore, with the theoretical volume expansion of Si/SiO_x-based anodes at 100–300%,^[71] $\text{SiO}_2\text{-CTAB@CNF}$ anodes only experienced 41% thickness expansion (Figure 4d,e), much smaller than $\text{SiO}_2\text{@CNF}$ (109%, Figure S13, Supporting Information). These results highlight the advantages of the spindle-like structure, in which the carbon coating serves as an intermediary buffering layer to mitigate the volume changes. This results in good structural stability during charge-discharge cycles.

To examine the practical application of $\text{SiO}_2\text{-CTAB@CNF}$ anode, a full-cell configuration was constructed by employing commercially available LiFePO₄ (LFP) as cathode material. Figure 4f illustrates the voltage profile of the $\text{SiO}_2\text{-CTAB@CNF} \parallel \text{LFP}$ full-cell battery under different areal current values. The full-cell battery delivers a high areal discharge capacity of 3.6 mAh cm^{-2} under 0.1 mA cm^{-2} with an initial coulombic efficiency (ICE) of 85%. This performance offers higher areal capacity than previously reported Si/SiO_x-based full-cell batteries (Table S4, Supporting Information).^[72–74] Increasing the areal current value to 0.2 and 0.3 mA cm^{-2} , the full-cell battery still maintains a high areal discharge capacity of 2.89 mAh cm^{-2} and 2.58 mAh cm^{-2} , respectively. Figure 4g depicts $\text{SiO}_2\text{-CTAB@CNF} \parallel \text{LFP}$ capable of maintaining stable areal capacity of 2.15 mAh cm^{-2} after 100 cycles at 0.3 mA cm^{-2} , equivalent to 83% of capacity retention. This capacity retention is comparable to or even outperforms previously reported full-cell Si/SiO_x batteries, which maintain 50–86% after 100 cycles and are mostly reported in low loading mass (Table S4, Supporting

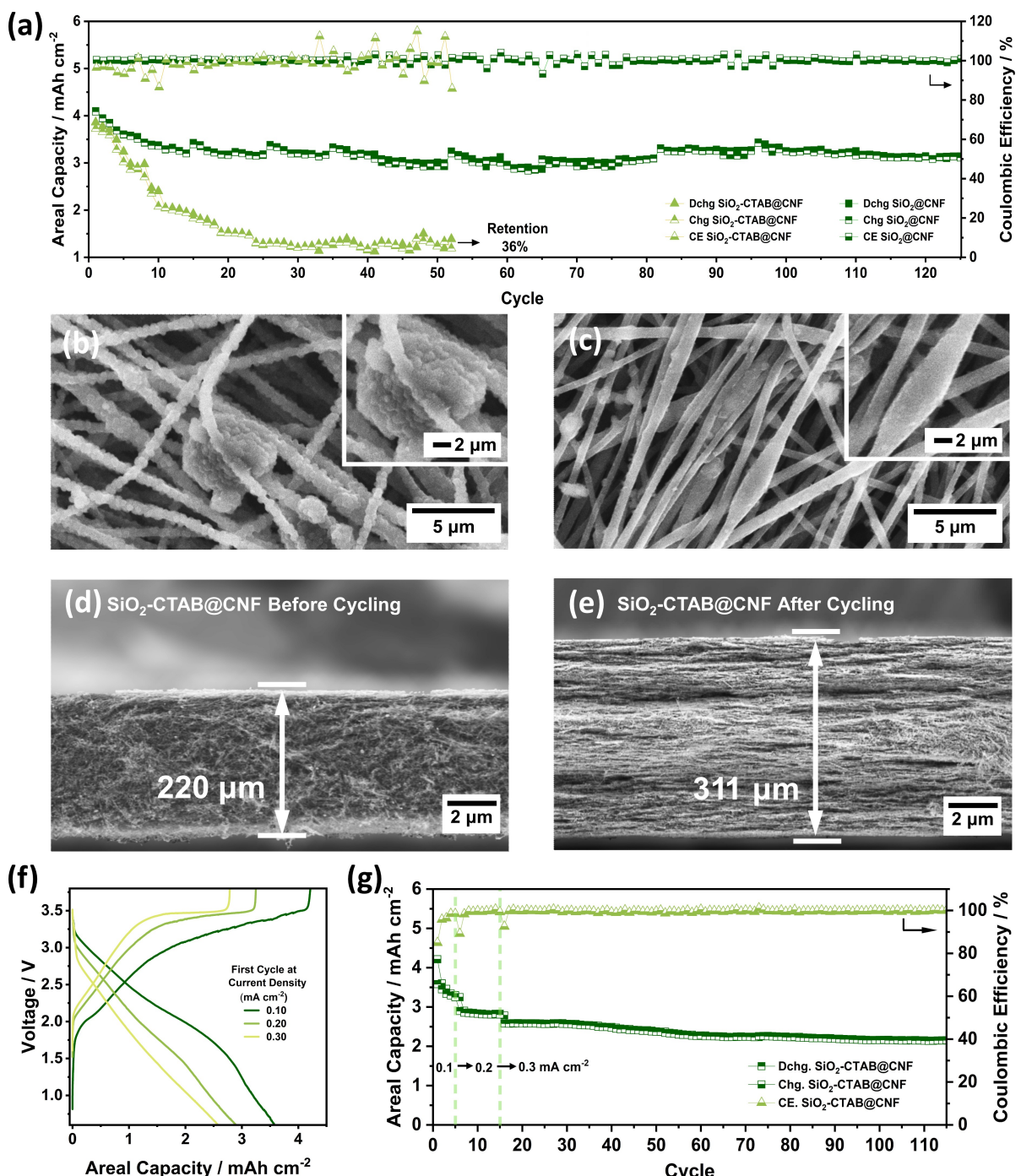


Figure 4. Charge-discharge performance evaluation of $\text{SiO}_2\text{@CNF}$ and $\text{SiO}_2\text{-CTAB@CNF}$ anode: (a) half-cell cycling stability with subsequent post-mortem SEM analysis of (b) $\text{SiO}_2\text{@CNF}$ and (c) $\text{SiO}_2\text{-CTAB@CNF}$ anode. Cross-sectional SEM analysis of $\text{SiO}_2\text{-CTAB@CNF}$ anode (d) before and (e) after cycling test. Full-cell battery performance of $\text{SiO}_2\text{-CTAB@CNF} \parallel \text{LFP}$: (f) voltage profile and (g) cycling stability under different areal current values.

Information).^[75–77] All in all, the performance of $\text{SiO}_2\text{-CTAB@CNF}$ in full-cell configuration proves its practical application in high-areal capacity Li-ion batteries.

Conclusions

In summary, self-supported anode with high areal capacity has been successfully fabricated from CTAB-treated SiO_2 nanoparticles obtained from geothermal waste. The high areal capacity can be achieved by constructing spindle-like silica-carbon nanofiber architectures via electrospinning. The interconnected spindle-like structures widen the gap between

nanofibers, producing higher porosity, low tortuosity, and effective electrolyte infiltration across the entire anode thickness. This structure also has good conductive networks, leading to fast charge transfer and high Li-ion diffusion. These features enable $\text{SiO}_2\text{-CTAB@CNF}$ to achieve a high areal capacity of 4 mAh cm^{-2} despite a substantial mass of 9.5 mg cm^{-2} , fulfilling the typical demands of high areal-capacity batteries. Post-mortem analysis also confirms the spindle-like structure's ability to suppress volume expansion of SiO_2 nanoparticles, leading to a high-stability $\text{SiO}_2\text{-CTAB@CNF}$ anode. Employing $\text{SiO}_2\text{-CTAB@CNF}$ anode in full-cell configuration with LFP cathode can achieve an impressive areal discharge capacity of 3.6 mAh cm^{-2} . The $\text{SiO}_2\text{-CTAB@CNF} \parallel \text{LFP}$ battery also still exhibits areal capacity of 2.58 mAh cm^{-2} at elevated areal current value of 0.3 mA cm^{-2} and retains 83% of its capacity after 100 cycles. This work demonstrates the significant potential of geothermal waste as high-performance lithium-ion battery anode materials.

Acknowledgements

The authors acknowledge the funding from Institut Teknologi Bandung through the 2024 ITB research program.

Conflict of Interests

The authors declare no conflict of interest.

Data Availability Statement

The data that support the findings of this study are available from the corresponding author upon reasonable request.

Keywords: Electrospinning • Li-ion batteries • Nanostructures • Nitrogen-doped carbon • Silicates

- [1] R. Dubey, M.-D. Zwahlen, Y. Shynkarenko, S. Yakunin, A. Fuerst, M. V. Kovalenko, K. V. Kravchyk, *Batteries & Supercaps* **2021**, *4*, 464–468.
- [2] Z. Liang, Y. Wang, B. Pei, S.-B. Son, M. Nguyen, N. R. Singstock, S. Huang, M. Mo, J. Li, M. S. Whittingham, C. Ban, *Adv. Energy Mater.* **2023**, *13*, 2301295.
- [3] Y. Kuang, C. Chen, D. Kirsch, L. Hu, *Adv. Energy Mater.* **2019**, *9*, 1901457.
- [4] C. Li, L. Zhu, S. Qi, W. Ge, W. Ma, Y. Zhao, R. Huang, L. Xu, Y. Qian, *ACS Appl. Mater. Interfaces* **2020**, *12*, 49607–49616.
- [5] L. Cheng, X. Sun, G. Wang, Y. Chen, Q. Zhu, P. Hu, W. Zhou, H. Wang, *Batteries & Supercaps* **2023**, *6*, e202200458.
- [6] L. A. Dold, C. R. Bapat, H. Gentischer, N. Ortlieb, A. Fischer, K. P. Birke, D. Biro, *Batteries & Supercaps* **2024**, *7*, e202400012.
- [7] M. Ashuri, Q. He, L. L. Shaw, *J. Power Sources* **2023**, *559*, 232660.
- [8] C. Eldona, N. Hanif Hawari, F. Haidar Hamid, W. Dempwolf, F. Iskandar, E. Peiner, H. Suryo Wasisto, A. Sumboja, *Chem. Asian J.* **2022**, *17*, e202200946.
- [9] F. H. Hamid, J. Karunawan, Y. Irmawati, B. T. Laksono, E. Peiner, H. S. Wasisto, F. Iskandar, A. Sumboja, *Electrochim. Acta* **2023**, *471*, 143384.
- [10] A. M. Firdaus, N. H. Hawari, C. G. Adios, P. M. Nasution, E. Peiner, H. S. Wasisto, A. Sumboja, *Chem. Asian J.* **2024**, *19*, e202400036.
- [11] Y.-W. Zhang, X.-T. Li, Y. Zhang, T.-T. Liu, M.-J. Fan, F.-H. Du, *J. Alloys Compd.* **2023**, *968*, 171831.
- [12] Y. Lu, Z. Zou, Y. Bai, X. Wang, H. Zhang, C. Jiang, *J. Energy Storage* **2023**, *72*, 108711.
- [13] X. Zhou, Y. Liu, P. Chen, X. Cao, D. Liu, R. Wang, *Ionics* **2023**, *29*, 2199–2208.
- [14] Z. Parviz, P. Salimi, S. Javadian, H. Gharibi, A. Morsali, E. Bayat, L. Leoncino, S. Lauciello, R. Proietti Zaccaria, *ACS Appl. Energ. Mater.* **2022**, *5*, 15155–15165.
- [15] H. Wu, L. Zheng, N. Du, B. Sun, J. Ma, Y. Jiang, J. Gong, H. Chen, L. Wang, *ACS Appl. Mater. Interfaces* **2021**, *13*, 22323–22331.
- [16] Y. Tzeng, C. Y. Jhan, K. M. Chiu, Y. C. Wu, G. Y. Chen, P. S. Wang, *Mater. Today Chem.* **2023**, *30*, 101570.
- [17] G. Mu, D. Mu, B. Wu, C. Ma, J. Bi, L. Zhang, H. Yang, F. Wu, *Small* **2020**, *16*, 1905430.
- [18] H. Wang, J. Fu, C. Wang, J. Wang, A. Yang, C. Li, Q. Sun, Y. Cui, H. Li, *Energy Environ. Sci.* **2020**, *13*, 848–858.
- [19] Q. Xu, C. Wu, X. Sun, H. Liu, H. Yang, H. Hu, M. Wu, *Nanoscale* **2021**, *13*, 18391–18409.
- [20] J. Yan, K. Dong, Y. Zhang, X. Wang, A. A. Aboalhassan, J. Yu, B. Ding, *Nat. Commun.* **2019**, *10*, 5584.
- [21] X. Li, W. Chen, Q. Qian, H. Huang, Y. Chen, Z. Wang, Q. Chen, J. Yang, J. Li, Y.-W. Mai, *Adv. Energy Mater.* **2021**, *11*, 2000845.
- [22] R. Akmalia, F. H. Hamid, F. D. Azura, Y. Irmawati, Q. Yan, A. Sumboja, *ACS Appl. Energ. Mater.* **2024**, *7*, 7064–7073.
- [23] C. Zhang, C. Ma, W. Zhang, Y. Wang, Z. U. Rehman, X. Shen, S. Yao, *Chem. Eng. J.* **2024**, *481*, 148374.
- [24] L. Li, P. Liu, K. Zhu, J. Wang, G. Tai, J. Liu, *Electrochim. Acta* **2017**, *235*, 79–87.
- [25] H. Wang, X. Yang, Q. Wu, Q. Zhang, H. Chen, H. Jing, J. Wang, S.-B. Mi, A. L. Rogach, C. Niu, *ACS Nano* **2018**, *12*, 3406–3416.
- [26] X. Li, K. Xu, Y. Yu, C. Chen, H. Zhang, W. Lei, *Electrochim. Acta* **2024**, *475*, 143658.
- [27] Q. Zhong, X. Yang, Z. Miao, L. Liu, Y. Xu, Y. Meng, Z. Yang, J. Yu, *Mater. Today Chem.* **2024**, *35*, 101919.
- [28] F. Shao, H. Li, L. Yao, S. Xu, G. Li, B. Li, C. Zou, Z. Yang, Y. Su, N. Hu, Y. Zhang, *ACS Appl. Mater. Interfaces* **2021**, *13*, 27270–27277.
- [29] M. Muraleedharan Pillai, N. Kalidas, X. Zhao, V.-P. Lehto, *Front. Chem.* **2022**, *10*, 882081.
- [30] S. Silviana, G. J. Sanyoto, A. Darmawan, H. Sutanto, *Rasayan J. Chem.* **2020**, *13*, 1692–1700.
- [31] M. Dirican, O. Yildiz, Y. Lu, X. Fang, H. Jiang, H. Kizil, X. Zhang, *Electrochim. Acta* **2015**, *169*, 52–60.
- [32] Y. Xu, K. Dong, Y. Jie, P. Adelhelm, Y. Chen, L. Xu, P. Yu, J. Kim, Z. Kochovski, Z. Yu, W. Li, J. LeBeau, Y. Shao-Horn, R. Cao, S. Jiao, T. Cheng, I. Manke, Y. Lu, *Adv. Energy Mater.* **2022**, *12*, 2200398.
- [33] J. Wang, C. Gao, Z. Yang, M. Zhang, Z. Li, H. Zhao, *Carbon Lett.* **2022**, *192*, 277–284.
- [34] S. Yao, H. Liu, C. Zhang, W. Zhang, C. Ma, Z. U. Rehman, X. Shen, *J. Energy Storage* **2024**, *78*, 110087.
- [35] Y. Aykut, B. Pourdeyhimi, S. A. Khan, *J. Appl. Polym. Sci.* **2013**, *130*, 3726–3735.
- [36] A. A. Aboalhassan, J. Yan, Y. Zhao, K. Dong, X. Wang, J. Yu, B. Ding, *iScience* **2019**, *16*, 122–132.
- [37] N. Saman, N. A. Ahmad Kamal, J. W. P. Lye, H. Mat, *Adv. Powder Technol.* **2020**, *31*, 3205–3214.
- [38] J. Cui, M. Wan, Z. Wang, Y. Zhao, L. Sun, *Sep. Purif. Technol.* **2023**, *321*, 124270.
- [39] A. Lakshmanan, D. S. Gavali, R. Thapa, D. Sarkar, *ACS Appl. Polym. Mater.* **2021**, *3*, 937–948.
- [40] C. Zhang, X. Yuan, L. Wu, Y. Han, J. Sheng, *Eur. Polym. J.* **2005**, *41*, 423–432.
- [41] K. Škrlec, Š. Zupančič, S. Prpar Mihevc, P. Kocbek, J. Kristl, A. Berlec, *Eur. J. Pharm. Biopharm.* **2019**, *136*, 108–119.
- [42] M. Liu, W. Xie, L. Gu, T. Qin, X. Hou, D. He, *Beilstein J. Nanotechnol.* **2016**, *7*, 1289–1295.
- [43] X. Lan, X. Zhou, Z. Jiao, H. Zong, P. Zhang, B. Xu, Y. Wang, *J. Alloys Compd.* **2024**, *972*, 172783.
- [44] W. Li, M. Li, K. R. Adair, X. Sun, Y. Yu, *J. Mater. Chem. A* **2017**, *5*, 13882–13906.
- [45] L. Si, K. Yan, C. Li, Y. Huang, X. Pang, X. Yang, D. Sui, Y. Zhang, J. Wang, C. Charles Xu, *Electrochim. Acta* **2022**, *404*, 139747.
- [46] Q. Aini, Y. Irmawati, J. Karunawan, M. H. R. Pasha, A. Alni, F. Iskandar, A. Sumboja, *Energy Fuels* **2023**, *37*, 11397–11405.
- [47] Y. Irmawati, D. A. Tan, F. Balqis, F. Iskandar, A. Sumboja, *Nanoscale* **2024**, *16*, 1833–1842.

- [48] Y. Liu, X. Wu, X. Guo, K. Lee, Q. Sun, X. Li, C. Zhang, Z. Wang, J. Hu, Y. Zhu, M. K. H. Leung, Z. Zhu, *Mater. Today Energy*. **2021**, *19*, 100610.
- [49] R. Akmalia, F. Balqis, M. F. Andriani, Y. Irmawati, A. Sumboja, *J. Energy Storage*. **2023**, *72*, 108743.
- [50] J. Y. Lee, N. Y. Kim, D. Y. Shin, H.-Y. Park, S.-S. Lee, S. Joon Kwon, D.-H. Lim, K. W. Bong, J. G. Son, J. Y. Kim, *J. Nanopart. Res.* **2017**, *19*, 98.
- [51] G. Lener, A. A. Garcia-Blanco, O. Furlong, M. Nazzarro, K. Sapag, D. E. Barraco, E. P. M. Leiva, *Electrochim. Acta*. **2018**, *279*, 289–300.
- [52] J. Chen, X. Zhou, M. Zhang, J. Wang, H. Li, J. Wang, C. Wang, *J. Alloys Compd.* **2022**, *902*, 163680.
- [53] G. Liu, X. Zhu, X. Li, D. Jia, D. Li, Z. Ma, J. Li, *J. Mater.* **2022**, *15*, 3190.
- [54] X.-Y. Zhang, Y. Zheng, C.-H. Liu, P.-H. Wang, Y.-Y. Zhu, *RSC Adv.* **2016**, *6*, 55666–55670.
- [55] M.-S. Wang, W.-L. Song, J. Wang, L.-Z. Fan, *Carbon Lett.* **2015**, *82*, 337–345.
- [56] X. Wang, N. Sun, X. Dong, M. Qi, H. Huang, *Chem. Asian J.* **2023**, *18*, e202201198.
- [57] J. Tang, X. Dai, F. Wu, Y. Mai, X. Wang, H. Jin, Y. Gu, Y. Xie, *Ionics*. **2020**, *26*, 639–648.
- [58] M. Zhang, J. Li, C. Sun, Z. Wang, Y. Li, D. Zhang, *J. Alloys Compd.* **2023**, *932*, 167687.
- [59] Y. Zhao, Z. Liu, Y. Zhang, A. Mentbayeva, X. Wang, M. Y. Maximov, B. Liu, Z. Bakenov, F. Yin, *Nanoscale Res. Lett.* **2017**, *12*, 459.
- [60] N. Sun, X. Wang, X. Dong, H. Huang, M. Qi, *Solid State Ionics* **2022**, *374*, 115817.
- [61] S. Qiu, Z. Huang, F. Fu, *Int. J. Hydrogen Energy*. **2024**, *91*, 1355–1364.
- [62] Z. Chen, T. Xiang, Q. Xiong, L. Chen, H. Yang, Z. Feng, X. Li, X. Shen, J. Huang, *Ionics* **2021**, *27*, 1385–1392.
- [63] X. Zhang, Z. Hui, S. King, L. Wang, Z. Ju, J. Wu, K. J. Takeuchi, A. C. Marsilok, A. C. West, E. S. Takeuchi, G. Yu, *Nano Lett.* **2021**, *21*, 5896–5904.
- [64] L. Li, R. M. Erb, J. Wang, J. Wang, Y.-M. Chiang, *Adv. Energy Mater.* **2019**, *9*, 1802472.
- [65] H. Wang, J. Li, Z. Miao, K. Huang, Y. Liao, X. Xu, J. Meng, Z. Li, Y. Huang, *ACS Appl. Mater. Interfaces*. **2023**, *15*, 26824–26833.
- [66] Q. Hu, X. Wang, Z. Wang, *Ceram. Int.* **2013**, *39*, 8487–8492.
- [67] R. Cong, J.-Y. Choi, J.-B. Song, M. Jo, H. Lee, C.-S. Lee, *Sci. Rep.* **2021**, *11*, 1283.
- [68] N. H. Hawari, H. Xie, A. Prayogi, A. Sumboja, N. Ding, *RSC Adv.* **2023**, *13*, 25673–25680.
- [69] M. Yu, B. Xin, Z. Chen, Y. Liu, *Fibers Polym.* **2023**, *24*, 4195–4202.
- [70] Y. Li, M. Zhang, X. Zhang, G. Xie, Z. Su, G. Wei, *Nanomaterials* **2015**, *5*, 1891–1905.
- [71] M. Jiao, Y. Wang, C. Ye, C. Wang, W. Zhang, C. Liang, *J. Alloys Compd.* **2020**, *842*, 155774.
- [72] V. Renman, M. V. Blanco, A. N. Norberg, F. Vullum-Bruer, A. M. Svensson, *Solid State Ionics* **2021**, *371*, 115766.
- [73] Y. Zeng, Y. Huang, N. Liu, X. Wang, Y. Zhang, Y. Guo, H.-H. Wu, H. Chen, X. Tang, Q. Zhang, *J. Energy Chem.* **2021**, *54*, 727–735.
- [74] C. Liu, Y. Liu, B. Wang, X. Liu, G. Wang, H. Wang, *J. Alloys Compd.* **2024**, *1009*, 176944.
- [75] K. Tian, Z. Song, Q. Zhou, C. Guan, M. Lu, M. Zhang, D. Wei, X. Li, J. Energy Storage. **2023**, *72*, 108401.
- [76] D. Guo, J. Wang, Y. Mai, P. Yang, J. Zhou, X. Xu, Y. Cheng, X. Dai, Y. Gu, F. Wu, *Ceram. Int.* **2023**, *49*, 5799–5807.
- [77] S. Mamidi, A. K. Pandey, A. D. Pathak, T. N. Rao, C. S. Sharma, *J. Alloys Compd.* **2021**, *872*, 159719.

Manuscript received: January 11, 2025

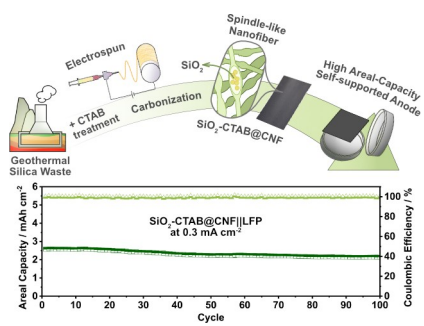
Revised manuscript received: February 5, 2025

Accepted manuscript online: February 6, 2025

Version of record online: ■■■, ■■■

RESEARCH ARTICLE

Self-supported spindle-like silica in carbon nanofiber ($\text{SiO}_2\text{-CTAB@CNF}$) was developed from CTAB-treated geothermal silica waste via electrospinning for high areal-capacity lithium-ion anode. The spindle-like structure balances high active material loading toward adequate porosity. Full-cell battery maintains stable high areal capacity (2.58 mAh cm^{-2}), reaching the targeted practical high areal-capacity lithium-ion battery.



F. Haidar Hamid, Y. Irmawati, A. Nur Estri, A. Hadziq Haidar, A. Sumboja*

1 – 10

High Areal Capacity Anode Enabled by Enhanced Charge Transport on Self-Supported Spindle-Like Carbon Nanofiber Architecture of CTAB-Treated Geothermal Silica Waste

